Dragging a defect in a droplet Bose-Einstein condensate

S. Saqlain,[1] Thudiyangal Mithun,[1] R. Carretero-González,[2] and P. G. Kevrekidis[1]
[1]*Department of Mathematics and Statistics, University of Massachusetts, Amherst, Massachusetts 01003-4515, USA*
[2]*Nonlinear Dynamical Systems Group, Computational Sciences Research Center, and Department of Mathematics and Statistics, San Diego State University, San Diego, California 92182-7720, USA*

(Received 12 September 2022; revised 21 February 2023; accepted 24 February 2023; published 10 March 2023)

In the present work we consider models of quantum droplets within a weakly interacting mass-balanced binary Bose-Bose mixture in the presence of a defect in the form of a laser beam moving through the respective condensates including the Lee-Huang-Yang correction. Our analysis features separately an exploration of the existence, stability, bifurcations, and dynamics in one-, two-, and three-dimensional settings. In the absence of an explicit solution of the problem, we provide an analysis of the speed of sound and observe how the states traveling with the defect may feature a saddle-center bifurcation as the speed or the strength of the defect is modified. Relevant bifurcation diagrams are constructed systematically and the unstable states, as well as the dynamics past the existence of stable states, are monitored. The connection of the resulting states with dark solitonic patterns in one dimension, vortical states in two dimensions, and vortex rings in three dimensions is accordingly elucidated.

DOI: 10.1103/PhysRevA.107.033310

I. INTRODUCTION

The study of atomic condensates has been a focal point at the interface of atomic, nonlinear optical, and wave physics during the past three decades since the experimental realization of Bose-Einstein condensates (BECs) of dilute alkali-metal gases [1,2]. From the nonlinear perspective, a wide array of studies has taken place in this context, ranging from the exploration of one-dimensional (1D) nonlinear waves in the form of dark solitons to 2D vortices and their lattices and finally in the 3D setting and the examination of vortex lines and rings [3].

A particular topic that has attracted considerable attention over the years, including in a wide range of experiments, has been the dragging of a defect (in the form of a light beam) through the condensate and the observation of the ensuing dynamics, especially so if the defect moves with a speed higher than the local speed of sound (violating the well-known Landau criterion) [4–6] and accordingly producing nonlinear excitations. Indeed, the relevant subject of both the associated instability and the resulting pattern formation has been of intense interest since early on [7–9] and continues to lead to variations on the relevant theme [10,11], e.g., involving trapping [12,13], for oscillating obstacles [14], in different dimensions [15], in periodic rings [16], for a larger number of components [17,18], or in the setting of polariton condensates involving dissipation and pumping processes [19] among many others, including recently beyond-mean-field effects [20].

On the other hand, a direction that has gained considerable traction lately has to do with the emergence of an effective new type of matter wave in the form of quantum droplets [21,22]. The relevant physical setting involves two-component (binary) BECs in which the effectively nonlinear interaction interplay involves intracomponent repulsion and intercomponent attraction (which slightly exceeds the former). It is in this system that the well-established Lee-Huang-Yang (LHY) quantum correction [23] can be used to incorporate the averaged beyond-mean-field effect of quantum fluctuations in the dynamical description while competing with the mean-field effects. A key role of the relevant correction is that of preventing the potential BEC collapse of the mean-field realm in higher dimensions. Such beyond-mean-field fluctuations have been found to be attractive in 1D settings, while they give a repulsive contribution to the interactions in dimensions greater than one.

A key appeal of these predictions and the associated study of quantum droplets is that they have led to a number of experimental implementations of this system [24–28], while such droplets were originally realized in dipolar settings [29,30]. Indeed, not only have individual droplets been observed but also their interactions in the form of collisions (both resulting in slow-collision mergers and in faster quasielastic events) have been reported for ^{39}K in Ref. [27]. Beyond homonuclear settings, heteronuclear droplets of ^{87}Rb and ^{41}K have also been shown to be long lived [28]. These substantial experimental findings have in turn motivated various theoretical studies such as the ones involving vortex clusters [31] and vortical droplets [32], the one of semidiscrete ones with or without vorticity [33], their dynamics in optical lattices [34], their modulational stability [35], or the case of 3D such structures in Ref. [36]. A relatively recent recap of theoretical and experimental activity in this field can be found in Ref. [37].

Our aim in the present work is to combine the above two central directions, namely, the study of the potential dragging in the form of a defect and the exploration of models of quantum droplets. An interesting feature of the latter models is their distinct yet well-established form in each of the three dimensions (one, two, and three) [37]. Here we explore, in the case of symmetric components, each one of these settings

separately, developing an analysis of the corresponding equilibrium states and obtaining the respective sound speeds as a function of the chemical potential. Subsequently, in the spirit of the work of Ref. [9], we consider a Gaussian defect (as a finite-width emulation of a δ-function one). We then use a systematic bifurcation analysis to explore the stable and unstable configurations pertaining to the moving defect, when such configurations exist (below the local speed of sound) as a function of the dragging speed and the defect strength. While in the case of the cubic nonlinear Schrödinger (NLS) model the existence of an explicit dark-soliton solution enables an analytical calculation of the relevant bifurcation curve, here the absence of such an analytical coherent structure expression leads us to identify the relevant curves numerically. We construct the corresponding two-parameter diagram and connect it with the speed of sound (to which the critical speed tends, as the height of the defect goes to 0). We perform such calculations for both one and higher (two and three) dimensions. In the latter, the systematic bifurcation curves present interesting features including an unstable branch bearing vortical states moving along with the defect. Interestingly, such states exist even for cubic nonlinearities. Finally, in three dimensions the vortex pairs are replaced by vortex ring structures which are moving with the defect, a pattern of interest in its own right.

Our presentation is structured as follows. In Sec. II we present the models at hand based on symmetric populations between the two components of the binary mixture. We also derive the speed of sound corresponding to the different dimensionalities. In Sec. III we present, for the 1D, 2D, and 3D settings, the corresponding equilibria and subsequently explore the bifurcation structure of stable and unstable states, the saddle-center bifurcation that they feature, and the corresponding dynamics for parameters both before and after the bifurcation. Section IV contains a summary of our findings and corresponding possible directions for future work. In the Appendices we revisit similar features for the cubic nonlinearity (higher-dimensional) case for completeness.

II. MODEL EQUATIONS THEORETICAL ANALYSIS

In the analysis that follows we focus our attention on the simpler, so-called symmetric, case where there is no population imbalance between the two components of the BEC binary mixture. Different aspects of asymmetric population mixtures in one, two, and three dimensions have been considered in Refs. [32,35,36], respectively. In three dimensions and under the assumption of symmetric populations and parameters, both BEC components are identical and can be described by a single wave function $\psi(\vec{r},t)$ satisfying the dimensionless Gross-Pitaevskii (GP) equation

$$i\partial_t\psi = -\tfrac{1}{2}\nabla^2\psi + \mathcal{N}(\psi) - \mu\psi + \mathcal{V}(\vec{r},t)\psi, \qquad (1)$$

where μ is the chemical potential, $\mathcal{V}(\vec{r},t)$ is the external potential, and $\mathcal{N}(\psi)$ is the effective nonlinearity. Note that in the symmetric case under consideration, μ, $\mathcal{V}(\vec{r},t)$, and $\mathcal{N}(\psi)$ are equal for both binary components. The crucial aspect when considering the LHY correction is that the effective nonlinearity deviates from the usual cubic one given by $|\psi|^2\psi$ and that it takes different forms depending on the effective dimensionality of the system [37]. In particular, for the different effective spatial dimensions the nonlinearity takes the form

$$\mathcal{N}(\psi) = \begin{cases} |\psi|^2\psi - |\psi|\psi & \text{in one dimension} \\ \ln(|\psi|^2)|\psi|^2\psi & \text{in two dimensions} \\ g_1|\psi|^2\psi + |\psi|^3\psi & \text{in three dimensions,} \end{cases} \qquad (2)$$

where g_1 can be positive or negative. These three cases will be considered herein.

We consider an impurity of fixed shape V moving across the BEC at velocity c in, without loss of generality, the x direction such that $\mathcal{V}(\vec{r},t) = V(x-ct,y,z)$. Thus, to be able to track steady states arising from the inclusion of the impurity, we cast the evolution equations in a comoving reference frame $\xi = x - ct$ where the impurity is stationary, yielding

$$i\partial_t A - ic\partial_x A = -\tfrac{1}{2}\nabla^2 A + \mathcal{N}(A) - \mu A + V(\vec{r})A, \qquad (3)$$

where we relabeled $\xi \to x$ and consider $A(x,y,z,t) = \psi(x-ct,y,z,t)$. We now study the different cases corresponding to one, two, and three dimensions.

A. One-dimensional setting

In practice, the BEC needs to be formed in the presence of a confining potential (in addition to the potential describing the running impurity). Provided this confining potential has very strong confinements in two directions, let us say along y and z, the dynamics of the BEC can be well approximated by the 1D version of the GP equation (3) [37]. In this quasi-1D case, where the transverse y and z directions have been factored (or better said, averaged) out, the BEC wave function $A(x)$, in the comoving reference frame, satisfies the (effective) 1D equation

$$i\partial_t A - ic\partial_x A = -\tfrac{1}{2}\partial_{xx}A + |A|^2A - |A|A - \mu A + V(x)A, \qquad (4)$$

where $V(x)$ now represents the 1D stationary profile of the running impurity in the comoving reference frame. The model (4) represents a binary condensate exhibiting an attractive intercomponent interaction g_{12} with an equal number of particles and equal repulsive intracomponent interaction strength ($g_1 = g_2$). This model could be implemented in an experiment by considering a mixture of ^{39}K atomic condensates in two different Zeeman states [25,38]. The units of length, time, wave function, and chemical potential are expressed in terms of the healing length ξ, $m\xi^2/\hbar$, $(2\sqrt{g})^{3/2}/\sqrt{\pi\xi}(2|\delta g|)^{3/4}$, and $\hbar^2/m\xi^2$, respectively, with $\xi = \frac{\pi\hbar^2}{m}\frac{\sqrt{2|\delta g|}}{g^{3/2}}$, $\delta g = g_{12} + g$, and $g = \sqrt{g_1 g_2}$ [39,40]. Accordingly, all the quantities depicted in the figures are dimensionless.

It is important to appreciate that the setting considered herein is reminiscent of the one in Ref. [33], aside from the presence of a longitudinal optical lattice in the latter. Hence, we can envision, in line with that work, a longitudinal size of the order of 10 μm, a gas of ^{39}K atoms, with atom numbers around 10^4 and a transverse trap of about $\omega_\perp = 2\pi \times 200$ Hz, while, when a longitudinal trap exists, the ratio of longitudinal to transverse trapping strengths is about 0.01 (see, e.g., Fig. 1 in Ref. [33]). This setting would be in line with the dynamical equations that appear, e.g., in Ref. [22], as well as

in Refs. [39,41], and the assumptions of $g_{11} \approx g_{22}$, in parallel with weak $\delta g > 0$ therein. Nevertheless, it is relevant to highlight here that Fig. S1 in Ref. [25] suggests the nontrivial challenge of leveraging a magnetic field in the vicinity of $B > 56.8$ G in order to achieve this goal. While this important question is outside the scope of the present study following the above setup, we want to highlight its relevance for further quantitative consideration in future studies.

In the homogeneous case, when the defect is absent, i.e., $V(x) = 0$, Eq. (1) admits a homogeneous, space-independent, stationary steady state $|A(\vec{r}, t)| = |\alpha|$ such that

$$|\alpha|^2 - |\alpha| - \mu = 0 \Rightarrow |\alpha| = \frac{1 \pm \sqrt{1 + 4\mu}}{2}, \tag{5}$$

where the solution with the minus sign exists for $-\frac{1}{4} < \mu < 0$, while the one with the plus sign exists for all $\mu > -\frac{1}{4}$. It is important to highlight here that the solution associated with the minus sign in Eq. (5) is modulationally unstable and is driven by the effectively attractive nature of the interactions within the LHY term. In what follows, we focus on the linearization around the modulationally stable state associated with the plus sign in Eq. (5). For the latter, the cubic repulsive interaction term dominates and the phenomenology resembles that of the standard NLS model [9], although with notable quantitative differences, as we now show. The most crucial ones among them are the concrete form of the relevant speed of sound that we will henceforth compute, as well as the fact that such a state (as well as the associated sound speed) is present even for $\mu < 0$, a feature absent in the purely cubic case of Ref. [9]. Looking now for comoving steady states for nonzero defects of Eq. (4) of the general form

$$A(x) = R(x)e^{i\phi(x)}, \tag{6}$$

where R and ϕ are real functions, yields

$$cR_x = \tfrac{1}{2}(2R_x\phi_x + R\phi_{xx}), \tag{7a}$$

$$cR\phi_x = -\tfrac{1}{2}\left(R_{xx} - R\phi_x^2\right) + R^3 - R^2 - \mu R + VR. \tag{7b}$$

Integrating Eq. (7a) yields

$$\phi_x = c\left(1 - \frac{|\alpha|^2}{R^2}\right),$$

which, after substituting in Eq. (7b) yields

$$R_{xx} = c^2\left(-R + \frac{|\alpha|^2}{R^3}\right) + 2R^3 - 2R^2 - 2\mu R + 2VR. \tag{8}$$

Since we assume that the defect is localized $V(x \to \pm\infty) \to 0$, we must require that $R(x) \to |\alpha|$ as $x \to \pm\infty$. Then, linearizing $R(x)$ as $R(x) = |\alpha| + r(x)$ for x away from the center yields

$$r_{xx} = 2r(|\alpha| + 2\mu - 2c^2), \tag{9}$$

implying that the speed of sound c_s for the 1D setting is given by

$$c_s = \sqrt{\frac{|\alpha| + 2\mu}{2}}, \tag{10}$$

in analogy with the cubic nonlinearity calculation of [9]. It should be noted that this relation (10) can also be obtained from the pressure $p = n^2\partial_n(E_{0v}/n)$, where the ground energy per volume is $E_{0v} = \frac{1}{2}n^2 - \frac{2}{3}n^{3/2}$ and $n = |\alpha|^2$ is the density [1]. Additionally, as per the Landau criterion [1,2], this represents the critical velocity required to create an excitation by a moving obstacle with velocity c through a uniform system.

It is important to highlight here that in Appendix D we provide a general derivation of the speed of sound. This derivation, based on the energy of elementary excitations presented in Refs. [1,2], is obtained for arbitrary nonlinearities in the NLS model and subsequently adapted to our model of interest herein. It is shown that the positive equilibrium state of Eq. (5) is associated with the positive speed of sound of Eq. (10). In contrast, the equilibrium with the minus sign, which is modulationally unstable and driven by the attractive interactions within the LHY term, has an imaginary speed of sound (as is the case, e.g., for cubic self-attractive NLS settings). The above statements are shown to be true for the positive state for arbitrary $\mu > -\frac{1}{4}$, while for the negative equilibrium state throughout its range of existence $-\frac{1}{4} < \mu < 0$.

B. Two-dimensional setting

Let us now consider the 2D setting. In this case, assuming a strong confinement in, let us say, the z direction and by appropriately averaging across this transverse direction, the 2D wave function in the comoving reference frame evolves according to [37]

$$i\partial_t A - ic\partial_x A = -\tfrac{1}{2}(\partial_{xx} + \partial_{yy})A + \ln(|A|^2)|A|^2 A - \mu A + V(x, y)A. \tag{11}$$

Note, importantly, that the nonlinearity, modified by the LHY correction term, assumes a somewhat unusual logarithmic form in the 2D setting. In this case, the homogeneous steady state $|A(\vec{r}, t)| = |\alpha|$ solves the transcendental equation

$$|\alpha|^2 \ln|\alpha|^2 - \mu = 0. \tag{12}$$

An analysis similar to the one done in one dimension (see Appendix A) yields the speed of sound for the 2D setting as

$$c_s = \sqrt{|\alpha|^2 + \mu}. \tag{13}$$

C. Three-dimensional setting

Finally, let us now consider the 3D setting. In this case, we use directly Eq. (1) in the comoving reference frame

$$i\partial_t A - ic\partial_x A = -\tfrac{1}{2}\nabla^2 A + g_1|A|^2 A + |A|^3 A - \mu A + VA, \tag{14}$$

where we have allowed the intrinsic cubic nonlinear term to be tuned from attractive $g_1 < 0$ to repulsive $g_1 > 0$. The homogeneous steady state $|A(\vec{r}, t)| = |\alpha|$ now yields a cubic equation for the amplitude:

$$|\alpha|^3 + g_1|\alpha|^2 - \mu = 0. \tag{15}$$

An analysis similar to the one done in one dimension (see Appendix B) yields the expression for the speed of sound in

the 3D setting

$$c_s = \sqrt{\frac{|\alpha|^3 + 2\mu}{2}}. \tag{16}$$

It is interesting to note that the expression for the speed of sound in Eq. (16) seems not to depend on the sign of g_1. Nonetheless, it is important to note that, although indeed Eq. (16) does not explicitly depend on g_1, it does so through the (dependence on g_1 of the) background level $|\alpha|$ as per Eq. (15).

We would like to point out that this 3D setting is possible in current cold-atom experiments [24,25]. In order to create a 3D droplet, one could consider around 10^5 atoms of ^{39}K in an external magnetic field of strength $B \sim 55$–56 G. The interaction parameters g_{11}, g_{22}, and g_{12} are functions of this external field B with values $g_{11} \sim 35a_0$, $g_{22} \sim 50a_0$, and $g_{12} \sim -50a_0$. These parameters keep the effective interaction parameter $\delta g = g_{12} + \sqrt{g_{11}g_{22}} < 0$. A Gaussian laser beam can be used to create the defect potential.

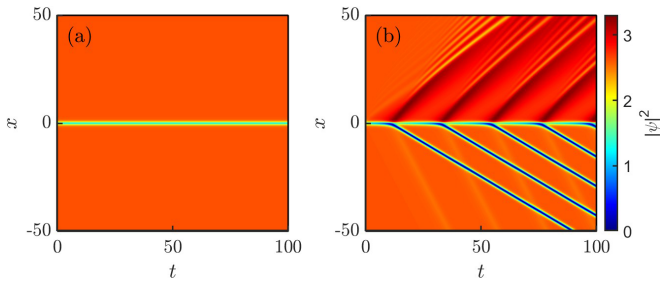

FIG. 1. Dynamics ensuing from a 1D defect running through the BEC for $\mu = 1$ ($|\alpha| \approx 1.62$) and $\lambda = 0.75$ ($c_{\rm crit} \approx 0.65$). (a) Subcritical case corresponding to a velocity $c = 0.647$ below the speed of sound. The resulting steady state is stable. (b) Supercritical case corresponding to a velocity $c = 0.7$ above the speed of sound. The resulting dynamics cannot feature a stationary state and consequently gives rise to a periodic emission of dark solitons in its wake. All quantities depicted in this figure and all subsequent figures are dimensionless.

III. NUMERICAL RESULTS

In this section we corroborate the predictions for the speed of sound of Sec. II and follow the different steady states and their dynamics for the different dimensionalities. For the numerical results, we use a standard finite-difference discretization of second order in space and fourth-order Runge-Kutta stepping in time. One-, two-, and three-dimensional results are typically obtained for domains $x \in [-200, 200]$, $(x, y) \in [-30, 30]^2$, and $(x, y, z) \in [-30, 30]^3$, respectively, with corresponding spatial discretizations such that lower dx was checked not to provide notable differences and a time step dt below the stability threshold given in Ref. [42]. The steady states are obtained by standard fixed-point iteration methods and the solution branches as parameters are varied were obtained using pseudoarclength continuation [43]. This methodology allows us to continue the solutions not only parametrically (e.g., over the speed) but also when they go around fold points, a feature typical of the results presented below. Rather than using a system parameter for the continuation, this approach uses the arclength (as the ideal parametrization and natural variable) of the bifurcation curve, enabling the continuation to bypass turning points, past which parametric continuation would fail. The bifurcation analysis presented has leveraged the use of the JULIA bifurcation package BIFURCATIONKIT [44], especially so for our 1D and 2D results. All the steady states and dynamics shown here are depicted in the comoving reference where the defect is stationary.

A. One-dimensional setting

For the 1D setting governed by Eq. (4), we consider a narrow Gaussian laser beam defect that runs through the condensate at velocity c. In the comoving reference frame, this 1D defect takes the form

$$V_{\rm 1D}(x) = \frac{\lambda}{\sqrt{2\pi\epsilon_x^2}} \exp\left(\frac{-x^2}{2\epsilon_x^2}\right),$$

where λ is the strength (intensity) of the defect and ϵ_x characterizes its waist (width). For our numerics, corresponding to the adimensionalized model of Eq. (4), we choose a chemical potential of $\mu = 1$ and a defect with waist $\epsilon_x = 0.2$.

For large enough c, namely, past the speed-of-sound threshold $c_{\rm crit}$, as it is the case for the pure cubic NLS nonlinearity without the LHY correction [9,15], the comoving steady state can no longer be supported (it has terminated in a saddle-center bifurcation, as we show below) and consequently emits a periodic train of dark solitons in its wake. Essentially, the emission of the solitary waves renders the dynamics temporarily and locally subcritical. However, once the solitary wave has moved enough upstream, the defect region becomes supercritical anew and yields an additional dark solitary structure, eventually resulting in the production of a train thereof. An example of this behavior is depicted in Fig. 1. Figure 1(a) shows how a defect running at low enough velocities gives rise to a stable comoving steady state. However, past a critical value of the speed, as shown in Fig. 1(b), this steady state disappears through a bifurcation as illustrated below, resulting in the production of a periodic train of dark solitons. As the speed of the defect is increased further the spacing between the dark soliton emissions decreases.

In order to numerically determine the critical speed for dark-soliton emission, we study the steady states that exist as the defect velocity is varied. In particular, as it is the case for the pure NLS case without the LHY correction (see, for instance, Ref. [9]), for values of c below the speed-of-sound threshold, there exist two steady-state solutions: A relatively shallow stable state and a relatively deep unstable steady state. For example, Fig. 2 depicts the evolution of the unstable solution for c below the speed of sound. This deeper solution decays, after the emission of a single dark soliton, to a shallower solution that precisely corresponds to the stable solution. We can now trace the families of unstable (deeper) and stable (shallower) solutions as the parameters of the system are varied. In particular, in Fig. 3 we follow, using pseudoarclength continuation in c, these solution branches for several values of the defect strength λ. To monitor the solutions, we

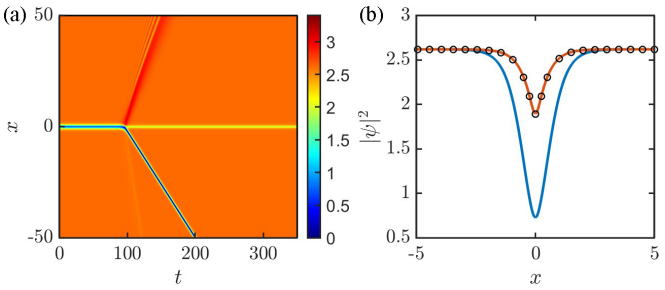

FIG. 2. Evolution of the 1D unstable solution for a defect velocity $c = 0.7$ below the speed of sound for $\mu = 1$ ($|\alpha| \approx 1.62$) and $\lambda = 0.4$ ($c_{\rm crit} \approx 0.85$). (a) Evolution where the deeper unstable steady-state solution sheds a single dark soliton and settles to an apparently stable shallower solution. (b) Plot confirming that the initial unstable steady state (blue curve) decays (after the emission of the single dark soliton) to a shallower solution (red curve) that precisely corresponds to the stable steady-state solution for this speed (circles).

use the effective mass of the solution

$$M_{\rm eff} = \int_{-\infty}^{+\infty} \left(|\alpha|^2 - |\psi|^2\right) dx, \tag{17}$$

where $|\alpha|$ is the background level as defined in Eq. (5). According to this definition, the deeper the solution, the higher the effective mass.

As can be seen in Fig. 3, the deep and shallow solutions, corresponding to the upper and lower solution branches, respectively, coalesce (see the turning point H) as the defect velocity c is increased. At a critical value of c, a saddle-center bifurcation ensues where the two solutions collide. Past this critical value of c, the system bears no stable solution and hence, as explained above, periodic emission of dark solitons takes place at the wake of the impurity as seen in Fig. 1(b). In Fig. 3 we also depict the theoretical prediction for the speed of sound of Eq. (10) (see the vertical black line). As seen in Fig. 3, the defects always have a critical speed that is below the speed of sound. This suggests that defects will emit dark-soliton trains for values slightly below the speed of sound. Nonetheless, the figure also suggests that the critical speed value tends to approach the speed of sound as the defect strength λ decreases. In fact, as the computation of the speed of sound in Sec. II relies on small perturbations, the results will be valid in the limit of $\lambda \to 0$. To elucidate this connection, we depict in Fig. 4 the values of the defect strength λ where the saddle-center collision between the deep and shallow steady states occurs. As it can be corroborated (see the inset), the critical velocity tends to coincide with the theoretical speed of sound c_s of Eq. (5) when the defect strength λ tends to zero. We have also produced the bifurcation diagram for negative values of μ, yielding qualitatively similar behavior (result not shown here) but with the localized structures attached to the impurity being wider.

Finally, within the one-dimensional setting, we also consider the case of a parabolically confining trap [45]. In particular, we are interested in the dynamics ensuing from moving a defect through a condensate confined by an external

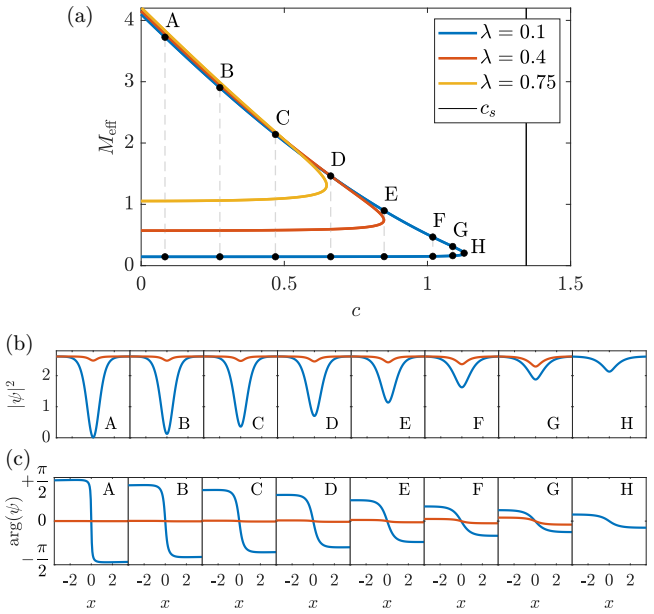

FIG. 3. (a) Bifurcation diagram for the stable (lower part of the corresponding branches) and unstable (upper part of the branches) branches in one dimension as the velocity of the impurity c is varied for $\mu = 1$ ($|\alpha| \approx 1.62$) and for three values of the impurity strength λ as indicated in the legend. The effective mass of the solution (see the text) is plotted vs c. As c reaches a threshold value, the upper and lower branches coalesce in a saddle-center bifurcation (see point H). For values of c larger than this threshold, there no longer exists a stable stationary state and hence the time evolution dynamics periodically sheds dark solitons in its wake [see Fig. 1(b)]. The vertical black line corresponds to the theoretical prediction of speed of sound in Eq. (10). Also shown are the corresponding (b) density and (c) phase profiles at the different values of c indicated by the black dots in (a). Each panel depicts the corresponding unstable (deep; see blue curve) and stable (shallow; see red curve) solutions.

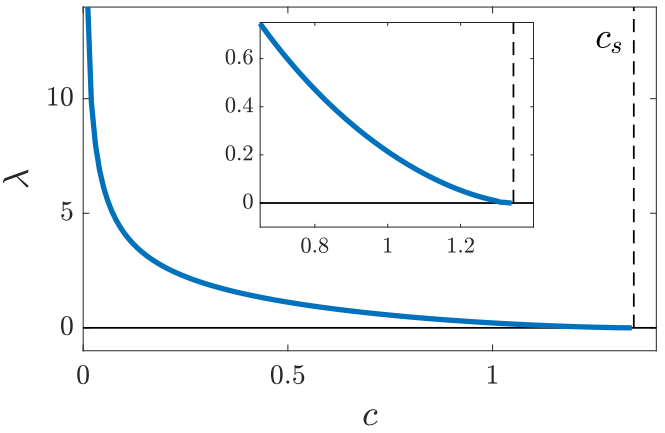

FIG. 4. Critical values of defect strength λ vs defect speed c for the 1D case. For each value of c we extract the value of λ where the saddle-center bifurcation occurs (collision between the deep and shallow steady-state solutions). The vertical dashed line corresponds to the theoretical prediction of the speed of sound in Eq. (5). The inset shows a zoomed-in version for small defect strengths.

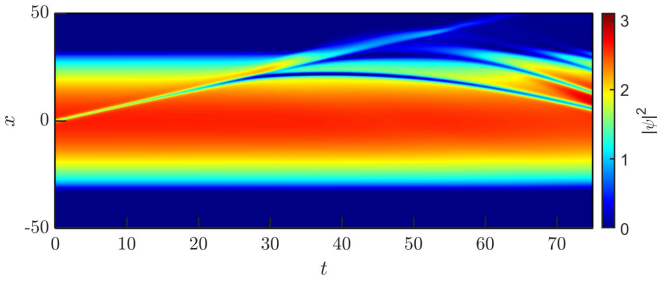

FIG. 5. Dynamics ensuing from a 1D defect running through the BEC confined in a parabolic trap for $\mu = 1.0$ ($|\alpha| \approx 1.62$), $\lambda = 0.5$ ($c_{\rm crit} \approx 0.78$), $c = 0.75$, and $\Omega = 0.05$. As the defect approaches the boundary of the condensate it gives rise to the emission of solitonic excitations.

(stationary) parabolic trap of the form

$$V_{\rm ext}(x) = \tfrac{1}{2}\Omega^2 x^2,$$

where Ω is the trap strength. Since there are no genuine traveling waves in the trapped setting, it is not possible to follow solutions in the cotraveling frame with the impurity. Therefore, we revert to the regime of Eq. (1) on a stationary frame. Importantly, in the trapped case, the density tends to zero at the edges of the condensate and thus the critical speed will be space dependent and crucially tend to zero as the impurity reaches the condensate edges. This means that, in principle, for *any* fixed impurity speed, as the impurity gets closer to the condensate edges, the local density will become sufficiently low to render the motion supercritical. Therefore, an impurity nearing the edges of the condensate will generally result in the ejection of solitary-wave excitations. This is precisely what we observed in our numerical experiments. Figure 5 presents the dynamics of a typical such case in this setting. Specifically, we start with a running impurity at the center of the condensate with a corresponding speed that is below the local (at the center) critical speed. As the impurity gets closer to the condensate edge, its (constant) speed becomes larger than the local (variable) critical speed and thus emits a few dark solitons. Eventually, the impurity leaves the condensate, while the emitted dark solitons oscillate and interact within the bulk of the trapped condensates (results not shown here).

B. Two-dimensional setting

We now proceed in a way similar to that for the 1D case of the preceding section but now for the 2D model of Eq. (11). Here we choose a 2D defect in the form of a bar that is thin in the direction of the defect movement (namely, the x direction) and relatively wide in the transverse direction. Specifically, the 2D defect is taken to be

$$V_{\rm 2D}(x, y) = V_{\rm 1D}(x) \exp\left(\frac{-y^2}{2\epsilon_y^2}\right).$$

Note that we do not use the typical normalization constant for a 2D Gaussian as we are considering the thin defect x direction the one that drives the nucleation of dark solitons and thus, to best compare with the 1D results, we use the same normalization prefactor as for the 1D case. For our numerical results

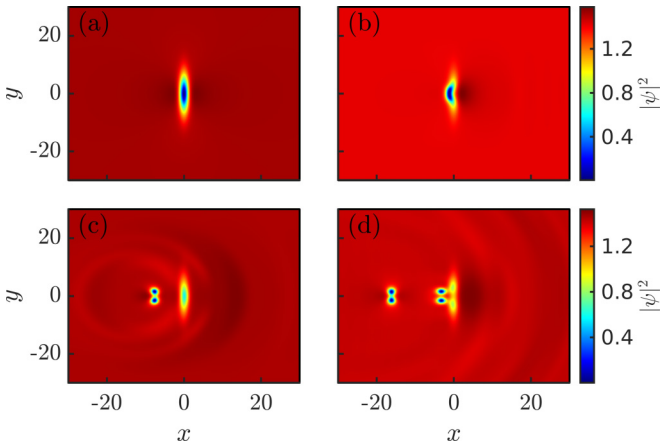

FIG. 6. Evolution corresponding to a supercritical 2D defect running at velocity $c = 0.8$ for $\mu = 0.5$ ($|\alpha| \approx 1.19$), $\lambda = 0.92$ ($c_{\rm crit} \approx 0.78$), and (a) $t = 0$, (b) $t = 20$, (c) $t = 35$, and (d) $t = 55$. The defect impurity periodically emits a vortex-antivortex pair in its wake (only two pairs shown here for $t \leqslant 55$).

below, we choose a thin defect bar with $\epsilon_x = 1/\sqrt{2} \approx 0.707$ and a relatively wide lateral extent with $\epsilon_y = 5$.

As in one dimension, for sufficiently large supercritical velocities, the 2D defect will not support a stable stationary state and will accordingly emit a periodic train in its wake. In the 2D case, the defect produces a train of vortex-antivortex pairs. A typical example depicting multiple vortex shedding instances is shown in Fig. 6 [larger times produce more vortex-antivortex shedding (results not shown here)]. Also, as in the 1D case, the 2D model also features two steady-state solutions for subcritical defect speeds: An unstable relatively deep one and a stable relatively shallow one. Figure 7 confirms, similar to what we saw for the 1D case, that for subcritical velocities, the deeper solution is unstable and, as it destabilizes, it sheds a *single* vortex-antivortex pair and eventually settles to the shallower stable steady state.

By monitoring the effective mass as in Eq. (17), but replacing the single x integral by an integral over the whole 2D domain and adjusting the background as per Eq. (12), we follow, using pseudoarclength continuation, the bifurcation diagram of subcritical 2D solutions. The resulting bifurcation diagram for $\mu = 0.5$ and for three different values of λ is depicted in Fig. 8. Interestingly, in this 2D case, the upper branch of steady-state solutions contains, for small enough values of the defect speed (namely, $c < 0.52$), a vortex-antivortex pair (see panels A–E). This is precisely the vortical structure pair that detaches from this unstable solution as it is evolved in time and finally settles to the corresponding stable lower branch solution, which in turn lacks any vortices (see, for instance, the dynamical evolution depicted in Fig. 7). It is also noteworthy that for small values of the running speed c, the steady-state vortex pair contains vortices that are relatively far away from the defect impurity (see, for instance, the profile in panel A which corresponds to a velocity $c = 0.025$). As c increases, the vortices of the upper branch solution get closer to the defect impurity. Further increasing c induces the vortices to get closer to each other within the impurity until they merge and disappear (in the present case of $\lambda = 0.92$ at an

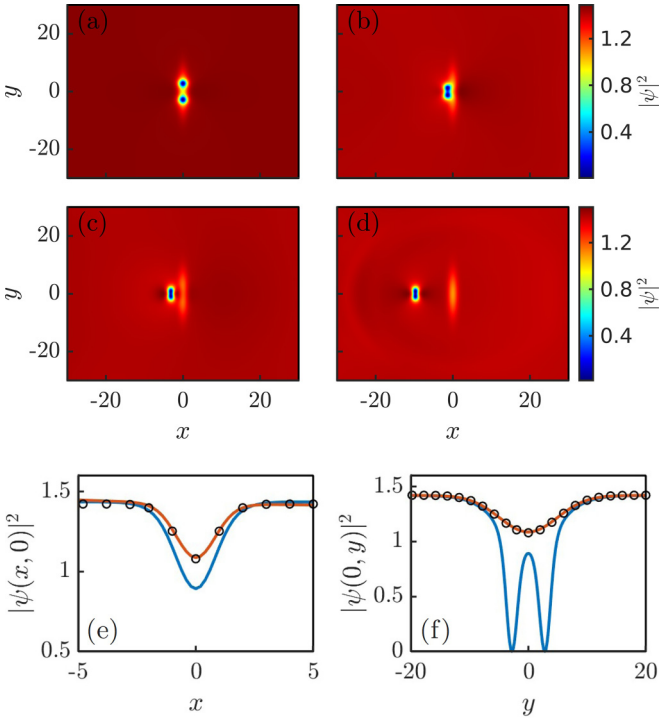

FIG. 7. Evolution of the 2D unstable solution for a defect velocity $c = 0.2$ below the speed of sound for $\mu = 0.5$ ($|\alpha| \approx 1.19$), $\lambda = 0.92$ $c_{\rm crit} \approx 0.78$, and (a) $t = 0$, (b) $t = 55$, (c) $t = 60$, and (d) $t = 75$. (a)–(d) show the evolution where the deeper unstable steady-state solution sheds a vortex-antivortex pair and settles to the stable shallower solution. Also shown are the (e) $x = 0$ and (f) $y = 0$ cuts of the density confirming that the initial unstable steady state (blue curves) decays (after the emission of the vortex pair) to a shallower solution (red curves) that precisely corresponds to the stable steady-state solution (shown by circles).

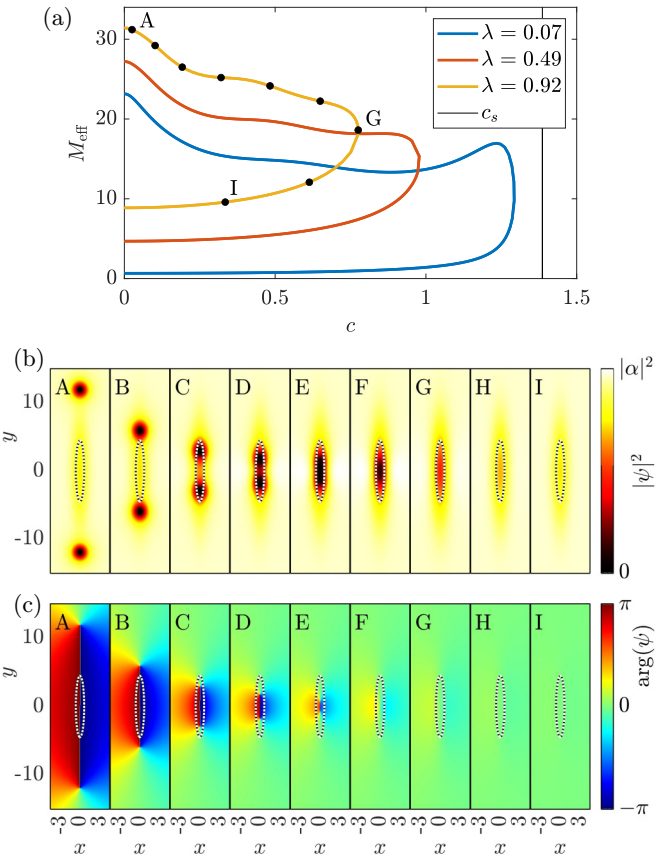

FIG. 8. (a) Similar to Fig. 3 but for the 2D case for $\mu = 0.5$ ($|\alpha| \approx 0.78$). The vertical black line corresponds to the theoretical prediction of speed of sound in Eq. (13). Also shown are the corresponding (b) density and (c) phase profiles at the different values of c indicated by the black dots in (a). The dashed curve represents the isocontour level of the potential $V_{\rm 2D}$ at $\frac{2}{3}$ of its maximum height.

approximate value of $c = 0.52$). Continuing past this vortex-merging point along the branch, the upper and lower solutions bifurcate from each other (or, equivalently, terminate) in a saddle-center bifurcation (case G in Fig. 8).

The astute reader may have noticed the oscillatory behavior of the effective mass for the upper branch solutions for small values of c in Fig. 8. This oscillatory behavior is missing in the 1D case (see the bifurcation curves in Fig. 3). We attribute these oscillations to the existence of the vortex pairs attached to the corresponding steady states. As the vortices move closer to the impurity and run through it when c is varied, they affect the effective mass and thus produce these small oscillations. In Fig. 9 we show the effects of varying the chemical potential μ on the upper branch steady state containing a pair of vortices attached at the end of the defect impurity. The existence of vortices for a wide range of μ values suggests that the above-mentioned oscillations of the effective mass will be visible for other values of the chemical potential. Additionally, the phenomenology discussed herein is present for different values of μ. However, the main feature that chiefly appears to change is the size of the vortices which shrinks, as the healing length shrinks for increasing μ. Moreover, for $\mu < 0$, we can observe an implication of the droplet nature of the configuration and the effective surface tension in such a setting, namely, a density modulation of the structure between the vortices, a feature far less noticeable in the cases of larger μ.

Finally, let us now compare the theoretical estimation of the speed of sound as per Eq. (13) and the critical value of the velocity in two dimensions. For this purpose, we depict in Fig. 10 the values of the defect strength λ where the saddle-center collision between the deep and shallow steady states occurs. As the inset corroborates, the critical velocity coincides reasonably well with the theoretical speed of sounds

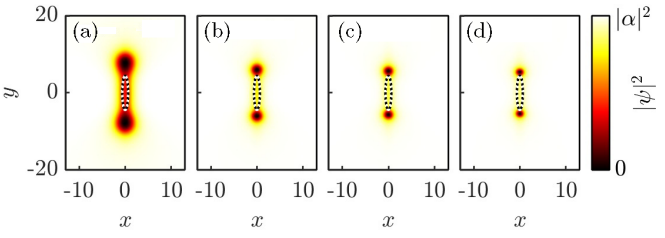

FIG. 9. Density profile of unstable solutions in the 2D case for $\lambda = 0.71$, $c = 0.1$, and (a) $\mu = -0.2$, (b) $\mu = 0.2$, (c) $\mu = 0.5$, and (d) $\mu = 1$. The dashed curve represents the isocontour level of the potential $V_{\rm 2D}$ at $\frac{2}{3}$ of its maximum height.

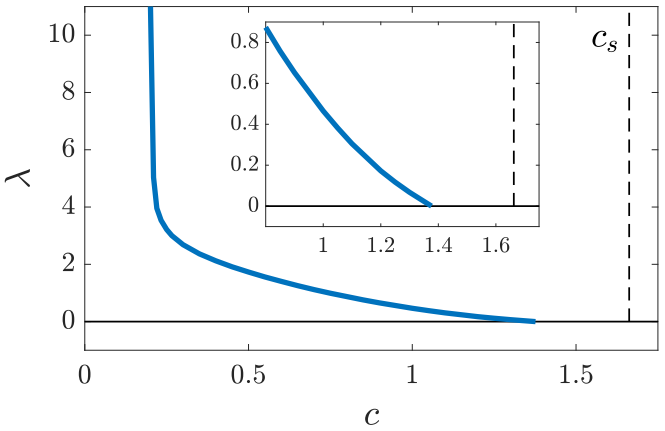

FIG. 10. Critical values of defect strength λ vs defect speed c for the 2D case. The layout is the same as in Fig. 4. The vertical dashed line corresponds to the theoretical prediction of the speed of sound in Eq. (12), which is tantamount to the limit of $\lambda \to 0$. The inset shows a zoomed-in version for small defect strengths.

c_s when the defect strength λ tends to zero, with the difference being attributable to the approximations within the numerical computations.

C. Three-dimensional setting

Let us now study the 3D model of Eq. (14). In this case we choose a defect impurity with the shape of a rectangular plate that is thin in the direction of the defect movement (namely, the x direction) and relatively wide in the other two transverse directions. Specifically, we use the 3D defect

$$V_{3D}(x, y, z) = V_{1D}(x) H_{w_z}(z) H_{w_y}(y),$$

with $\epsilon_x = \frac{1}{4}$, $w_y = 8$, and $w_z = 4$ and where H_w is a smoothed 1D top-hat function given by

$$H_w(r) = \frac{1}{4}\left[\tanh\left(\frac{w}{2} + r\right) + 1\right]\left[\tanh\left(\frac{w}{2} - r\right) + 1\right].$$

As it was the case for the 1D and 2D settings above, we take a relatively thin Gaussian profile in the direction of motion. In the transverse directions we take a relatively large (when compared to the thin longitudinal direction) rectangular plate. One of the motivations to use a rectangular plate is to observe the effects of this anisotropy in the transverse directions. Naturally, an isotropic, namely, circular, defect plate would give rise to a perfectly isotropic steady-state solution, which in turn, when supersonic, would nucleate a symmetric vortex ring (results not shown here).

Similarly to what we observe in the 1D and 2D cases, the 3D model also gives rise to two branches of subcritical steady-state solutions. These two solution branches correspond to unstable, relatively large (when compared to the size of the defect), vortex rings and stable density depletions. We monitor the effective mass as in Eq. (17), but replace the single x integral by an integral over the whole 3D domain and adjust the background as per Eq. (15). As before, we use pseudoarclength continuation to follow these branches of subcritical 3D steady-state solutions. The results for $g_1 = 1$ and $\mu = 0.5$ are depicted in Fig. 11 for three different values

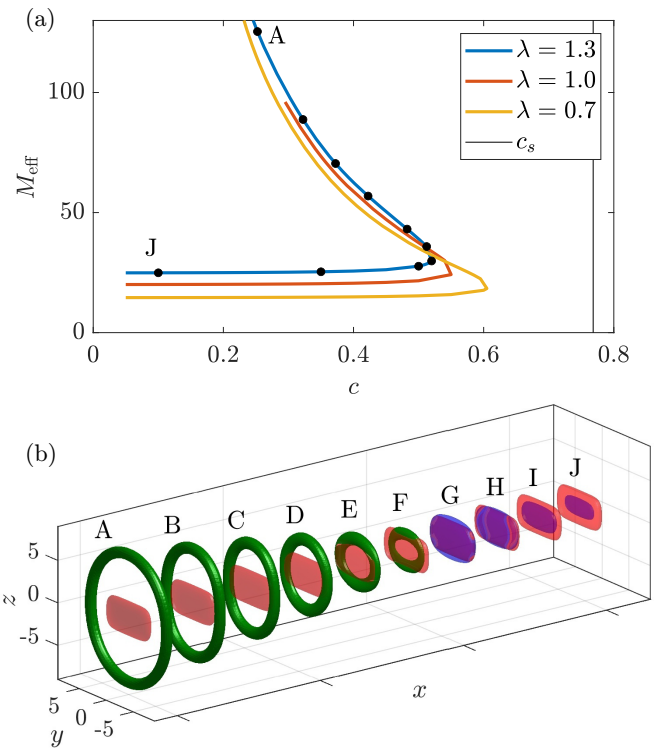

FIG. 11. (a) Bifurcation diagram for the stable and unstable branches in three dimensions for $g_1 = 1$, $\mu = 0.5$ ($|\alpha| \approx 0.56$), and the values of λ indicated in the legend. The layout and meaning are similar to those in Fig. 3. The vertical black line corresponds to the theoretical prediction of the 3D speed of sound in Eq. (16). (b) Corresponding profiles at the different values of c indicated by the black dots in (a). Each instance depicts an isocontour of the corresponding vorticity (solid green) together with an isocontour of the 3D defect potential V_{3D} at $\frac{1}{2}$ of its maximum amplitude (transparent red). The points corresponding to G–J do not carry a sizable amount of vorticity and thus isocontours of the density are shown instead (transparent blue).

of the defect strength λ. It is interesting to notice that in the limit of small defect speed c, the upper branch of unstable solutions corresponds to large vortex rings that are larger than, and seemingly detached from, the impurity. On the other hand, the stable steady states, corresponding to density depletions that do not carry vorticity, are tightly attached to the defect. This provides a physical explanation for their corresponding stability as the larger ring, being farther away from the defect, detaches through the instability. On the other hand, the smaller density depletion is tightly attached to the impurity and is found to be dynamically stable. Another interesting feature is that for intermediate values of the velocity, the vortex ring has an aspect ratio opposite to that of the defect plate. See, for instance, the vortex ring corresponding to the points B and C which are taller than wider, while the defect is, oppositely, wider than taller. Therefore, the effect of the anisotropy of the defect plate is to typically create vortex rings that lack circular symmetry and that are slightly "squeezed" in the horizontal or vertical direction. This is to be contrasted with the case of a circular plate that would nucleate a perfectly symmetric circular steady state and in turn shed a symmetric

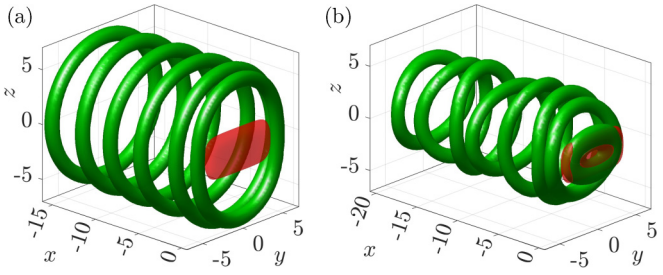

FIG. 12. Examples of vortex ring emission from the unstable steady-state solution. Each panel depicts overlaid snapshots of the vorticity (green surfaces) at different times during the emission of a single vortex ring from the defect (shown in red) on a comoving reference frame. The ensuing dynamics are from cases (a) B and (b) F in Fig. 11, namely, for $\lambda = 1.3$ ($c_{\rm crit} \approx 0.52$), $\mu = 0.5$ ($|\alpha| \approx 0.56$), $g_1 = 1$, and (a) $c = 0.3224$ (case B) and (b) $c = 0.5124$ (case F). The times for the snapshots for cases B and F are, respectively, $t = \{0, 160, 220, 280, 340, 400\}$ and $t = \{0, 90, 100, 120, 140, 160, 180, 200\}$, from the closest vortex ring to the defect to the one farthest away.

vortex ring (results not shown here). The asymmetry present in the unstable steady state is inherited by the vortex rings that are nucleated from the unstable subcritical steady state as well as the train of vortex rings that are nucleated from the defect impurity running at supercritical speeds. This asymmetry means that the vortex rings nucleated by the defect will contain Kelvin (vibrational) modes [46,47] that will induce internal oscillations (see Fig. 12).

Let us now follow in more detail on the nucleation of vortex rings from the unstable branch of solutions. In particular, we depict in Fig. 12 the evolution of the unstable steady states corresponding to cases B [Fig. 11(a)] and F [Fig. 11(b)]. The simulations depict how the vortex ring, which is pinned by the defect, detaches (by virtue of the solution's instability) and then travels downstream. It is worth recalling that, as per our setup in Sec. II, mounting is always in a comoving reference frame on top of the running defect. As mentioned above, the pinned vortex rings are asymmetric as per our choice of defect that has a rectangular transverse (i.e., perpendicular to its motion) cross section. Therefore, the detaching vortex rings are not circular and thus are prone to Kelvin, internal, oscillatory modes. It is also interesting to note that the larger vortex rings, corresponding to relatively small values of the running defect speed c, detach and keep their relatively large radius [cf. case B in Fig. 12(a)]. On the other hand, for larger defect speeds, the pinned vortex ring has a small radius and thus expands as it detaches [cf. case F in Fig. 12(b)]. It is also worth mentioning that the detached vortex rings do not travel downstream at velocity c with the background fluid velocity. This is because the detached vortices (and also the nucleated vortices for supercritical speeds) have an intrinsic velocity v_i that goes *against* the background flow (see Ref. [48] and references therein). Thus, vortex rings do travel downstream but with a slower velocity than the background flow corresponding to $c - v_i$.

Finally, since it may be physically relevant to consider negative values of g_1 in the 3D model (14), we depict in Fig. 13 the bifurcation diagram for the steady-state solutions

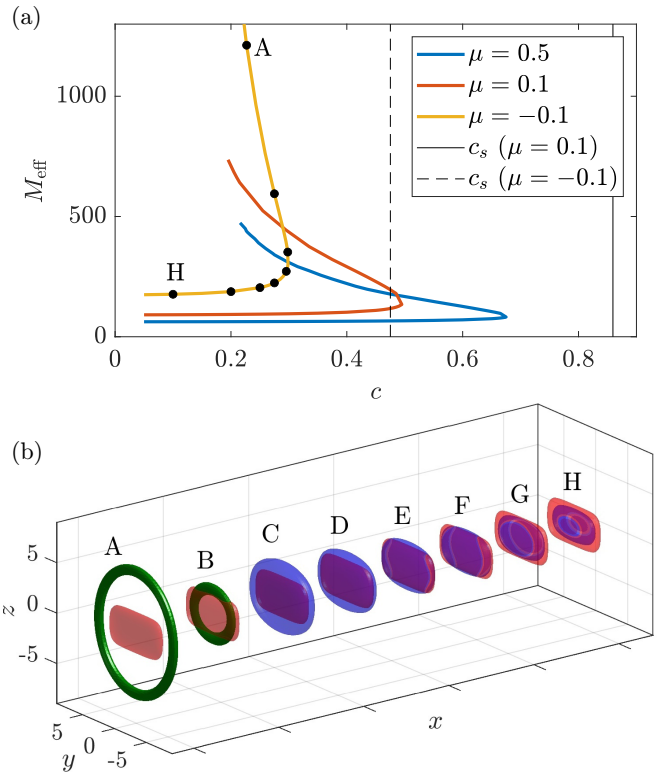

FIG. 13. Same as in Fig. 11 but for constant $\lambda = 1.3$ and $g_1 = -1$ for the values of μ indicated in the legend. In this case, the points corresponding to C–H do not carry a sizable amount of vorticity and thus density isocontours are shown instead.

for $g_1 = -1$ and a defect strength of $\lambda = 1.3$ for three different values of the chemical potential μ. The results are similar as the ones presented for $g_1 = 1$ in Fig. 11 with no significant qualitative differences.

IV. CONCLUSIONS AND FUTURE CHALLENGES

We have studied the effects of running an impurity defect through a Bose-Einstein condensate in a regime that takes into account the incorporation of the Lee-Huang-Yang correction that gives rise to quantum droplets. We systematically explored the 1D, 2D, and 3D cases that feature different nonlinear LHY corrections. For all dimensionalities, we followed, using pseudoarclength continuation, the two subcritical solution branches that exist for defect velocities below the critical speed and which feature a localized waveform cotraveling with the defect. These solutions correspond to dark solitons, vortex-antivortex pairs, and vortex rings for the 1D, 2D, and 3D cases, respectively. In all cases we find that there exist an upper and a lower branch of solutions connected through a saddle-center bifurcation. The upper branch is found to always be unstable and corresponds to a solution that has a relatively larger effective mass and a nonlinear state further detached from the defect. In contrast, the lower solution branch of relatively smaller effective mass is dynamically stable for subcritical velocities and features a state more closely bound to the defect. When dynamically evolved, the solution on the upper branch always destabilizes by shedding a single coherent

structure and then settling to its lower branch, stable, sibling solution. By using a perturbation approach, we were able to theoretically predict the corresponding speed of sound of the medium, which in turn takes a different functional form for the different model dimensionalities. We corroborated that the theoretically computed speed of sounds does match the bifurcation point (where the upper and lower branches collide) as the strength of the defect tends to zero and we identified how this critical speed (as well as the corresponding saddle-center bifurcation point) deviates, i.e., decreases from this threshold, as we move into the finite defect strength case. In the 3D case we showcased the effect of using an anisotropic defect in the transverse direction. This anisotropy is responsible for the formation of squeezed vortex rings again featuring a similar bifurcation diagram. We explored the relevant phenomenologies not only as a function of the dragging speed and the defect strength, but also in terms of the chemical potential variations, observing the variation of the states as the droplet (negative chemical potential) limit is approached. Finally, we also performed dynamics in the supercritical case, observing how the disappearance of the states cotraveling with the defect results in the emission of a train of dark solitons, or a street of vortices or an array of vortex rings in one, two, and three dimensions, respectively.

The present work naturally suggests numerous additional considerations in the context of nonlinear wave patterns embedded in the types of droplet models that were considered herein. While some studies along this vein have recently taken place both in one dimension [49,50] and in higher dimensions [37], it appears that a detailed understanding of dark solitons, vortices, or vortex pairs and vortex rings embedded within droplet configurations is largely still missing, as is a characterization of their stability and dynamics. We believe that such a systematic study and also comparison with beyond-mean-field models (for a recent review see Ref. [51]) would be of particular interest in future work.

ACKNOWLEDGMENTS

This material is based upon work supported by the U.S. National Science Foundation under the awards PHY-2110038 (R.C.-G.) and PHY-2110030 and DMS-2204702 (P.G.K.).

APPENDIX A: SPEED OF SOUND IN TWO DIMENSIONS

Looking for solutions to Eq. (11) of the form of Eq. (6) but in two dimensions yields

$$cR_x = \tfrac{1}{2}(2R_x\phi_x + R\phi_{xx} + 2R_y\phi_y + R\phi_{yy}), \tag{A1}$$

$$cR\phi_x = -\tfrac{1}{2}\left(R_{xx} + R_{yy} - R\phi_x^2 - R\phi_y^2\right) + R^3\ln R^2 - \mu R + VR. \tag{A2}$$

Further linearizing and expanding the phase and density terms by using transverse modes of wave number k in the y direction as $\phi(x,y,t) = \epsilon\theta(x,t)e^{iky}$ and $R(x,y,t) = |\alpha| + \epsilon r(x,t)e^{iky}$, Eqs. (A1) and (A2) become

$$2cr_x = |\alpha|(\theta_{xx} - k^2\theta), \tag{A3}$$

$$r_{xx} = -2c|\alpha|\theta_x + r(k^2 + 4|\alpha|^2 + 4\mu). \tag{A4}$$

Finally, by making the substitutions $r = ae^{\Lambda x}$ and $\theta = be^{\Lambda x}$, Eqs. (A1) and (A2) read

$$M\begin{bmatrix} a \\ b \end{bmatrix} = \begin{bmatrix} 0 \\ 0 \end{bmatrix},$$

where

$$M = \begin{bmatrix} 2c\Lambda/|\alpha| & k^2 - \Lambda^2 \\ k^2 + 4|\alpha|^2 + 4\mu - \Lambda^2 & -2|\alpha|\Lambda \end{bmatrix}.$$

Then, setting $\det(M) = 0$ with $k = 0$ and $\Lambda = 0$ yields the speed of sound for the 2D setting as

$$c_s = \sqrt{|\alpha|^2 + \mu}. \tag{A5}$$

We test this prediction numerically under different settings in Sec. III B.

APPENDIX B: SPEED OF SOUND IN THREE DIMENSIONS

Looking for solutions to Eq. (11) of the form of Eq. (6) but now in three dimensions yields

$$2cR_x = 2R_x\phi_x + R\phi_{xx} + 2R_y\phi_y + R\phi_{yy} + 2R_z\phi_z + R\phi_{zz}, \tag{B1}$$

$$cR\phi_x = -\tfrac{1}{2}\left(R_{xx} - R\phi_x^2 + R_{yy} - R\phi_y^2 + R_{zz} - R\phi_z^2\right) + R^4 + g_1R^3 - \mu R + VR. \tag{B2}$$

As in the 2D calculations, we now allow the density and phase terms to contain transverse modes. In this case, we include modes in the y and z directions as $\phi(x,y,z,t) = \epsilon\theta(x,t)e^{ik_yy}e^{ik_zz}$ and $R(x,y,t) = |\alpha| + \epsilon r(x,t)e^{ik_yy}e^{ik_zz}$. Then, after linearization, Eqs. (B1) and (B2) become

$$2cr_x = |\alpha|\left[\theta_{xx} - \left(k_y^2 + k_z^2\right)\theta\right], \tag{B3}$$

$$r_{xx} = r\left[2|\alpha|^3 + 4\mu + \left(k_y^2 + k_z^2\right)\right] - 2c|\alpha|\theta_x. \tag{B4}$$

Using the substitutions $r = ae^{\Lambda x}$ and $\theta = be^{\Lambda x}$ yields the linear system

$$M\begin{bmatrix} a \\ b \end{bmatrix} = \begin{bmatrix} 0 \\ 0 \end{bmatrix},$$

where

$$M = \begin{bmatrix} 2c\Lambda/|\alpha| & \left(k_y^2 + k_z^2\right) - \Lambda^2 \\ \left(k_y^2 + k_z^2\right) + 2|\alpha|^3 + 4\mu - \Lambda^2 & -2c|\alpha|\Lambda \end{bmatrix}.$$

Finally, setting $\det(M) = 0$, $k_y = k_z = 0$, and $\Lambda = 0$ yields the expression for the speed of sound in the 3D setting

$$c_s = \sqrt{\frac{|\alpha|^3 + 2\mu}{2}}. \tag{B5}$$

APPENDIX C: SPEED OF SOUND FOR THE NLS CASE

For comparison with the LHY case and for completeness, the next two sections show the results of the pure NLS model case

$$i\partial_t A - ic\partial_x A = -\tfrac{1}{2}\nabla^2 A + |A|^2 A - \mu A + VA, \tag{C1}$$

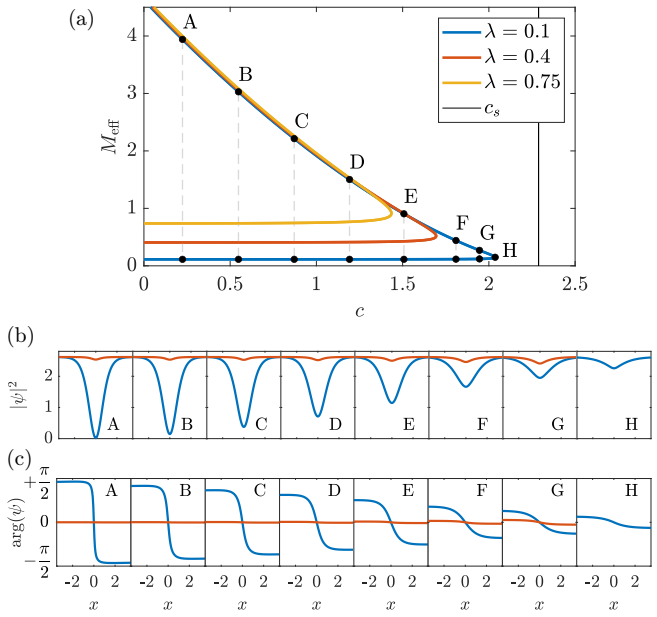

FIG. 14. Same as in Fig. 3 but for the standard (cubic) NLS model (C1) in one dimension without the LHY correction. The value of $\mu = |\alpha|^2$ was chosen here so as to match the background density supporting the dark solitons for the LHY case. In this case, the theoretical prediction for the speed of sound is given by Eq. (C4). Note the similarity to the results of the LHY case in Fig. 3, albeit with a different scale on the c axis.

with ∇^2 the Laplacian and V the corresponding defect potential. In contrast to the case with the LHY correction, the pure NLS model admits a single homogeneous steady state of density $|\alpha|^2 = \mu$.

1. The NLS case in one dimension

Analyzing this case in a way similar to that in Sec. II A, indeed following the work of Ref. [9], after replacing $A(x) = R(x)e^{i\phi(x)}$, the system

$$\phi_x R^2 = cR^2 + C_I, \tag{C2}$$

$$cR\phi_x = -\tfrac{1}{2}\left(R_{xx} - R\phi_x^2\right) + R^3 - \mu R + VR, \tag{C3}$$

with the constant of integration $C_I = -c\mu$. Solving for ϕ_x in Eq. (C2) and replacing in it in Eq. (C3) yields

$$R_{xx} = c^2\left(-R + \frac{\mu^2}{R^3}\right) + 2R^3 - 2\mu R + 2VR.$$

Linearizing as before, using $R(x) = |\alpha| + r(x)$, yields the expression for the evolution of the perturbation

$$r_{xx} = r(\mu - c^2)$$

and therefore the speed of sound in one dimension for the pure NLS case is given by

$$c_s = \sqrt{\mu}. \tag{C4}$$

The relevant calculation both in this section and in the next one is provided for reasons of completeness.

Figure 14 depicts the numerical results corresponding to the standard 1D NLS model (C1). These results are to be compared with the corresponding ones in Fig. 3 that include the LHY correction as per Eq. (4). When comparing the two cases at first glance, little difference is observed. However, note the quite different scales of defect speeds c such that the velocities for the standard NLS case are about twice those with the LHY correction.

2. The NLS case in two dimensions

Following an analysis very similar to the one in Sec. II B and Appendix A yields, after (i) separating the density and phase by $A(x, y, t) = R(x, y, t)e^{i\phi(x,y,t)}$, (ii) expanding in transversal modes by using $\phi(x, y, t) = \epsilon\theta(x, t)e^{iky}a$, (iii) linearizing the perturbed solution using $R(x, y, t) = r_0 + \epsilon r(x, t)e^{iky}$, and (iv) some algebra, yields, to first order, the system

$$\frac{2cr_x}{r_0} = \theta_{xx} - k^2\theta, \tag{C5}$$

$$r_{xx} = -2cr_0\theta_x + r(k^2 + 4\mu). \tag{C6}$$

Then, making the substitutions $r = ae^{\lambda x}$ and $\theta = be^{\lambda x}$ yields a new set of equations, which can be written as the matrix system

$$\begin{bmatrix} \frac{2c\lambda}{r_0} & k^2 - \lambda^2 \\ k^2 + 4\mu - \lambda^2 & -2cr_0\lambda \end{bmatrix}\begin{bmatrix} a \\ b \end{bmatrix} = \begin{bmatrix} 0 \\ 0 \end{bmatrix}.$$

Setting the determinant equal to zero then yields the characteristic polynomial

$$-\lambda^4 + \lambda^2(-4c^2 + 2k^2 + 4\mu) - k^2(k^2 + 4\mu) = 0,$$

which implies that, for the most unstable mode $k = 0$, the speed of sound for the standard NLS model in two dimensions is given by

$$c_s = \sqrt{\mu}. \tag{C7}$$

Figure 15 depicts the numerical results corresponding to the standard 2D NLS model (C1). These results are very similar to the corresponding ones in Fig. 8 that include the LHY correction as per Eq. (11). As it was the case for the droplet model, the NLS also displays a nonmonotonic behavior of the effective mass as c decreases for the upper branch. We again attribute this behavior to the appearance of the vortices that start, for small c, far away from the impurity and then get closer to it as c increases [see Fig. 15(b)].

APPENDIX D: SPEED OF SOUND FOR ARBITRARY NONLINEARITY

Let us consider the Landau criterion [1,2], indeed, for a general nonlinear Schrödinger (i.e., GP) equation of the form

$$iu_t = -\tfrac{1}{2}u_{xx} + f(u) - \mu u, \tag{D1}$$

where μ plays the role of the chemical potential, while $f(u)$ plays the role of the nonlinearity here, with $f(u) = |u|^2u$ for the standard GP equation, while $f(u) = |u|^2u - |u|u$ for our droplet setting. Given that we are examining excitations around the positive homogeneous states of the system, we (for this calculation) set $f(u) = u^3$ in the former case, while $f(u) = u^3 - u^2$ in the latter.

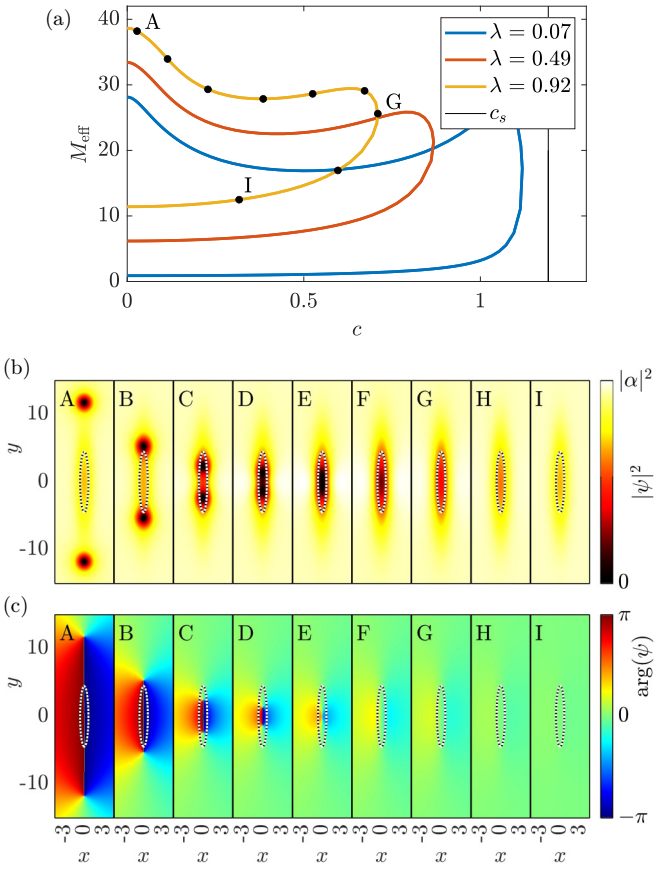

FIG. 15. Similar to Fig. 8 but for the standard NLS 2D model without the LHY correction. The vertical line in (a) is the predicted speed of sound for the pure NLS in two dimensions given by Eq. (C7).

Performing the standard Bogoliubov–de Gennes analysis [1,2] (but for this general nonlinearity), we find that the energies (frequencies) of excitation around such a homogeneous state will satisfy the dispersion relation

$$\omega^2 = \frac{k^2}{2}\left(\frac{k^2}{2} + (f'(u) - \mu)\right).$$

Then, forming the relevant ratio of ω/k, we find

$$\frac{\omega}{k} = \frac{1}{2}\sqrt{k^2 + 2[f'(u) - \mu]}, \tag{D2}$$

and hence the minimization dictated by the Landau criterion [1,2], to obtain the associated speed of sound, occurs at $k = 0$ and yields the general formula

$$c_s = \tfrac{1}{2}\sqrt{2[f'(u) - \mu]}. \tag{D3}$$

It is relevant to first verify that for $f(u) = u^3$ in the standard cubic GP equation for which $f'(u) = 3u^2 = 3\mu$ for the homogeneous state, we obtain from the above calculation the well-known result that $c_s = \sqrt{\mu}$, discussed also in Appendix C.

Now, turning to our droplet model case, it is relevant to understand the relevant criterion *both* for the positive and for the negative states and to ensure that it is relevant to consider even in the regime of negative chemical potentials. Therefore, we consider now $f(u) = (u^2 - u)u = \mu u$, which leads to our positive and negative states $u = (1 \pm \sqrt{1 + 4\mu})/2$ and find that $f'(u) = 3u^2 - 2u = u^2 + 2(u^2 - u) = u^2 + 2\mu$, given that the positive and negative equilibria satisfy $u^2 - u = \mu$. This in turn leads from Eq. (D2) directly to

$$c_s = \sqrt{\frac{u^2 + \mu}{2}} = \sqrt{\frac{u + 2\mu}{2}}. \tag{D4}$$

The first observation is that this is in perfect alignment, as it should be, with the expression previously derived in Eq. (10), i.e., the Landau criterion is still valid and consonant with our earlier calculation.

More importantly, let us explore the specifics of the relevant expression and its suitability for the regime of negative chemical potentials ($\mu > -\frac{1}{4}$) and for the positive and negative states. From the exact solution for the positive and negative states, we have that

$$u + 2\mu = \tfrac{1}{2}(1 + 4\mu \pm \sqrt{1 + 4\mu}) \equiv \tfrac{1}{2}(y \pm \sqrt{y}), \tag{D5}$$

where we have set $y = 1 + 4\mu$, which naturally is greater than 0 for $\mu > -\frac{1}{4}$, i.e., in the regime of chemical potentials of interest. This expression is especially informative because in the regime of negative chemical potentials $\mu < 0$, $0 < 1 + 4\mu = y < 1$. Accordingly, in this regime it is true that $y < \sqrt{y}$. Hence, for the positive branch, the quantity under the radical of Eq. (D4), i.e., the expression in Eq. (D5), is positive and hence the speed of sound is real. In contrast, for the negative state, the modulationally unstable (attractive-interaction-dominated) state, the quantity inside the radical $y - \sqrt{y}$, turns out to be negative and hence the speed of sound is imaginary, exactly as is the case, e.g., for attractive condensates with the attractive cubic nonlinearity.

Naturally, the considerations presented here are provided for the 1D case, but it is a straightforward algebraic exercise to confirm that they extend naturally (as they should) for the 2D and 3D cases presented in our work. The role of the trap has been argued in many publications, including, e.g., Refs. [14–18], to be a modulation of the density, hence a local modification of the speed of sound. This results in the feature that even if dragging the relevant defect is subcritical near the trap center, there will always be a density such that for fixed dragging speed, the system will become supercritical when crossing the region of such a density and thus lead to emission of excitations.

[1] C. J. Pethick and H. Smith, *Bose-Einstein Condensation in Dilute Gases* (Cambridge University Press, Cambridge, 2008).

[2] S. Stringari and L. Pitaevskii, *Bose-Einstein Condensation* (Oxford University Press, Oxford, 2003).

[3] P. G. Kevrekidis, D. J. Frantzeskakis, and R. Carretero-González, *The Defocusing Nonlinear Schrödinger Equation: From Dark Solitons to Vortices and Vortex Rings* (Society for Industrial and Applied Mathematics, Philadelphia, 2015).

[4] C. Raman, M. Köhl, R. Onofrio, D. S. Durfee, C. E. Kuklewicz, Z. Hadzibabic, and W. Ketterle, Evidence for a Critical Velocity in a Bose-Einstein Condensed Gas, Phys. Rev. Lett. **83**, 2502 (1999).

[5] R. Onofrio, C. Raman, J. M. Vogels, J. R. Abo-Shaeer, A. P. Chikkatur, and W. Ketterle, Observation of Superfluid Flow in a Bose-Einstein Condensed Gas, Phys. Rev. Lett. **85**, 2228 (2000).

[6] P. Engels and C. Atherton, Stationary and Nonstationary Fluid Flow of a Bose-Einstein Condensate Through a Penetrable Barrier, Phys. Rev. Lett. **99**, 160405 (2007).

[7] T. Frisch, Y. Pomeau, and S. Rica, Transition to Dissipation in a Model of Superflow, Phys. Rev. Lett. **69**, 1644 (1992).

[8] T. Winiecki, J. F. McCann, and C. S. Adams, Pressure Drag in Linear and Nonlinear Quantum Fluids, Phys. Rev. Lett. **82**, 5186 (1999).

[9] V. Hakim, Nonlinear Schrödinger flow past an obstacle in one dimension, Phys. Rev. E **55**, 2835 (1997).

[10] P. Leboeuf and N. Pavloff, Bose-Einstein beams: Coherent propagation through a guide, Phys. Rev. A **64**, 033602 (2001).

[11] N. Pavloff, Breakdown of superfluidity of an atom laser past an obstacle, Phys. Rev. A **66**, 013610 (2002).

[12] V. A. Brazhnyi and A. M. Kamchatnov, Creation and evolution of trains of dark solitons in a trapped one-dimensional Bose-Einstein condensate, Phys. Rev. A **68**, 043614 (2003).

[13] I. Hans, J. Stockhofe, and P. Schmelcher, Generating, dragging, and releasing dark solitons in elongated Bose-Einstein condensates, Phys. Rev. A **92**, 013627 (2015).

[14] A. Radouani, Soliton and phonon production by an oscillating obstacle in a quasi-one-dimensional trapped repulsive Bose-Einstein condensate, Phys. Rev. A **70**, 013602 (2004).

[15] R. Carretero-González, P. G. Kevrekidis, D. J. Frantzeskakis, B. A. Malomed, S. Nandi, and A. R. Bishop, Soliton trains and vortex streets as a form of Cerenkov radiation in trapped Bose-Einstein condensates, Math. Comput. Simul. **74**, 361 (2007).

[16] M. Syafwan, P. Kevrekidis, A. Paris-Mandoki, I. Lesanovsky, P. Krüger, L. Hackermüller, and H. Susanto, Superfluid flow past an obstacle in annular Bose-Einstein condensates, J. Phys. B **49**, 235301 (2016).

[17] H. Susanto, P. G. Kevrekidis, R. Carretero-González, B. A. Malomed, D. J. Frantzeskakis, and A. R. Bishop, Čerenkov-like radiation in a binary superfluid flow past an obstacle, Phys. Rev. A **75**, 055601 (2007).

[18] A. S. Rodrigues, P. G. Kevrekidis, R. Carretero-González, D. J. Frantzeskakis, P. Schmelcher, T. J. Alexander, and Y. S. Kivshar, Spinor Bose-Einstein condensate flow past an obstacle, Phys. Rev. A **79**, 043603 (2009).

[19] P.-E. Larré, N. Pavloff, and A. M. Kamchatnov, Wave pattern induced by a localized obstacle in the flow of a one-dimensional polariton condensate, Phys. Rev. B **86**, 165304 (2012).

[20] G. C. Katsimiga, S. I. Mistakidis, G. M. Koutentakis, P. G. Kevrekidis, and P. Schmelcher, Many-body dissipative flow of a confined scalar Bose-Einstein condensate driven by a Gaussian impurity, Phys. Rev. A **98**, 013632 (2018).

[21] D. S. Petrov, Quantum Mechanical Stabilization of a Collapsing Bose-Bose Mixture, Phys. Rev. Lett. **115**, 155302 (2015).

[22] D. S. Petrov and G. E. Astrakharchik, Ultradilute Low-Dimensional Liquids, Phys. Rev. Lett. **117**, 100401 (2016).

[23] T. D. Lee, K. Huang, and C. N. Yang, Eigenvalues and eigenfunctions of a Bose system of hard spheres and its low-temperature properties, Phys. Rev. **106**, 1135 (1957).

[24] C. R. Cabrera, L. Tanzi, J. Sanz, B. Naylor, P. Thomas, P. Cheiney, and L. Tarruell, Quantum liquid droplets in a mixture of Bose-Einstein condensates, Science **359**, 301 (2018).

[25] P. Cheiney, C. R. Cabrera, J. Sanz, B. Naylor, L. Tanzi, and L. Tarruell, Bright Soliton to Quantum Droplet Transition in a Mixture of Bose-Einstein Condensates, Phys. Rev. Lett. **120**, 135301 (2018).

[26] G. Semeghini, G. Ferioli, L. Masi, C. Mazzinghi, L. Wolswijk, F. Minardi, M. Modugno, G. Modugno, M. Inguscio, and M. Fattori, Self-Bound Quantum Droplets of Atomic Mixtures in Free Space, Phys. Rev. Lett. **120**, 235301 (2018).

[27] G. Ferioli, G. Semeghini, L. Masi, G. Giusti, G. Modugno, M. Inguscio, A. Gallemí, A. Recati, and M. Fattori, Collisions of Self-Bound Quantum Droplets, Phys. Rev. Lett. **122**, 090401 (2019).

[28] C. D'Errico, A. Burchianti, M. Prevedelli, L. Salasnich, F. Ancilotto, M. Modugno, F. Minardi, and C. Fort, Observation of quantum droplets in a heteronuclear bosonic mixture, Phys. Rev. Res. **1**, 033155 (2019).

[29] L. Chomaz, S. Baier, D. Petter, M. J. Mark, F. Wächtler, L. Santos, and F. Ferlaino, Quantum-Fluctuation-Driven Crossover from a Dilute Bose-Einstein Condensate to a Macrodroplet in a Dipolar Quantum Fluid, Phys. Rev. X **6**, 041039 (2016).

[30] I. Ferrier-Barbut, H. Kadau, M. Schmitt, M. Wenzel, and T. Pfau, Observation of Quantum Droplets in a Strongly Dipolar Bose Gas, Phys. Rev. Lett. **116**, 215301 (2016).

[31] M. N. Tengstrand, P. Stürmer, E. O. Karabulut, and S. M. Reimann, Rotating Binary Bose-Einstein Condensates and Vortex Clusters in Quantum Droplets, Phys. Rev. Lett. **123**, 160405 (2019).

[32] Y. Li, Z. Chen, Z. Luo, C. Huang, H. Tan, W. Pang, and B. A. Malomed, Two-dimensional vortex quantum droplets, Phys. Rev. A **98**, 063602 (2018).

[33] X. Zhang, X. Xu, Y. Zheng, Z. Chen, B. Liu, C. Huang, B. A. Malomed, and Y. Li, Semidiscrete Quantum Droplets and Vortices, Phys. Rev. Lett. **123**, 133901 (2019).

[34] I. Morera, G. E. Astrakharchik, A. Polls, and B. Juliá-Díaz, Quantum droplets of Bosonic mixtures in a one-dimensional optical lattice, Phys. Rev. Res. **2**, 022008(R) (2020).

[35] T. Mithun, A. Maluckov, K. Kasamatsu, B. A. Malomed, and A. Khare, Modulational instability, inter-component asymmetry, and formation of quantum droplets in one-dimensional binary Bose gases, Symmetry **12**, 174 (2020).

[36] Y. V. Kartashov, B. A. Malomed, L. Tarruell, and L. Torner, Three-dimensional droplets of Swirling superfluids, Phys. Rev. A **98**, 013612 (2018).

[37] Z. Luo, W. Pang, B. Liu, Y. Li, and B. A. Malomed, A new form of liquid matter: Quantum droplets, Front. Phys. **16**, 32201 (2021).

[38] S. Roy, M. Landini, A. Trenkwalder, G. Semeghini, G. Spagnolli, A. Simoni, M. Fattori, M. Inguscio, and G. Modugno, Test of the Universality of the Three-Body Efimov Parameter at Narrow Feshbach Resonances, Phys. Rev. Lett. **111**, 053202 (2013).

[39] G. E. Astrakharchik and B. A. Malomed, Dynamics of one-dimensional quantum droplets, Phys. Rev. A **98**, 013631 (2018).

[40] T. Mithun, S. I. Mistakidis, P. Schmelcher, and P. G. Kevrekidis, Statistical mechanics of one-dimensional quantum droplets, Phys. Rev. A **104**, 033316 (2021).

[41] M. Tylutki, G. E. Astrakharchik, B. A. Malomed, and D. S. Petrov, Collective excitations of a one-dimensional quantum droplet, Phys. Rev. A **101**, 051601(R) (2020).

[42] R. Caplan and R. Carretero-González, Numerical stability of explicit Runge-Kutta finite-difference schemes for the nonlinear Schrödinger equation, Appl. Numer. Math. **71**, 24 (2013).

[43] E. J. Doedel, in *Numerical Continuation Methods for Dynamical Systems: Path Following and Boundary Value Problems*, edited by B. Krauskopf, H. M. Osinga, and J. Galán-Vioque (Springer, Dordrecht, 2007), pp. 1–49.

[44] R. Veltz, BifurcationKit.jl, available at https://bifurcationkit.github.io/BifurcationKitDocs.jl/stable/ (2020).

[45] M. Pathak and A. Nath, Dynamics of quantum droplets in an external harmonic confinement, Sci. Rep. **12**, 6904 (2022).

[46] T. P. Simula, T. Mizushima, and K. Machida, Vortex waves in trapped Bose-Einstein condensates, Phys. Rev. A **78**, 053604 (2008).

[47] F. Chevy and S. Stringari, Kelvin modes of a fast rotating Bose-Einstein condensate, Phys. Rev. A **68**, 053601 (2003).

[48] R. M. Caplan, J. D. Talley, R. Carretero-González, and P. G. Kevrekidis, Scattering and leapfrogging of Vortex rings in a superfluid, Phys. Fluids **26**, 097101 (2014).

[49] Y. V. Kartashov, V. M. Lashkin, M. Modugno, and L. Torner, Spinor-induced instability of kinks, holes and quantum droplets, New J. Phys. **24**, 073012 (2022).

[50] M. Edmonds, Dark quantum droplets in beyond-mean-field Bose-Einstein condensate mixtures, arXiv:2209.00790.

[51] S. I. Mistakidis, A. G. Volosniev, R. E. Barfknecht, T. Fogarty, T. Busch, A. Foerster, P. Schmelcher, and N. T. Zinner, Cold atoms in low dimensions—A laboratory for quantum dynamics, arXiv:2202.11071.